

# A Hybrid Finite Element Method for Axisymmetric Waveguide fed Horns \*

G.C. Chinn, D.J. Hoppe, and L.W. Epp<sup>†</sup>  
Jet Propulsion Laboratory  
California Institute of Technology  
Pasadena, CA 91109

## Abstract

A new method for finding radiation patterns and the reflection coefficients associated with an axisymmetric waveguide fed horn is presented. The approach is based on a hybrid finite element method (FEM) wherein the electromagnetic fields in the FEM region are coupled to the fields outside by two surface integral equations. Because of the local nature of the FEM, this formalism allows for the presence of inhomogeneities to be included in the problem domain. The matrix equation which results from the application of this method is shown to be complex-symmetric. It is, furthermore, diagonally dominant and sparse. Comparisons of calculated and measured data for two different horns show good agreement.

## 1. INTRODUCTION

The problem of finding radiation patterns and the reflection coefficients of an axisymmetric waveguide fed horn is clearly important to designers as this kind of horn is used both as an antenna and as a feed. Although design principles for many of the specific horns of this type are well known- for instance, a corrugated horn [1,2], dielectric rod [3], and dielectric horn [4]- a tool with more accurate predictive powers is often needed. This is especially true for those horns which use a combination of design rules such as the feed horn shown in Fig. 1. This horn features a flange section, a dielectric surface-wave element, and is covered by a radome.

In the absence of inhomogeneities, an approach which can find the desired quantities was developed by Berthon and Bills [5] using the method of moments (MoM) in conjunction with a single waveguide mode serving as the sole excitation for the fields. Their method, while yielding very accurate reflection coefficients and radiation patterns, does not apply to horns with inhomogeneities due to the fact that their integral equation kernels are derived from free

\* This work was performed at the Jet Propulsion Laboratory, California Institute of Technology under a contract with the National Aeronautics and Space Administration.

<sup>†</sup>The authors are with the Jet Propulsion Laboratory, California Institute of Technology, 4800 Oak Grove Drive, Pasadena, CA 91109.

space Green's functions. As is well known, however, the finite element method (FEM) can address problems with inhomogeneities. Consequently, this paper will present a FEM formulation which solves the problem of radiation from axisymmetric waveguide fed horns with or without inhomogeneities in-scent.

In this approach, the FEM is coupled to both the MoM and a modal technique via surface integrals. The FEM region contains all the inhomogeneities. The FEM/MoM boundary serves to couple the local FEM electromagnetic fields to the external radiated fields. This type of FEM/MoM coupling has been used previously for scattering problems [6,7] and it is on the particular approach given in [7], the Hybrid Symmetric Finite Element Method (HSFEM), that this present work is based. The FEM/modal boundary, on the other hand, provides a means for waveguide modes to excite the local FEM fields thus transforming the technique from one that solves scattering problems to one that addresses radiation problems. Following [7, 8], we describe, in section III, this FEM/modal coupling. It is noted that the FEM/modal hybridization has its roots in the waveguide discontinuity problem [9, 10] wherein modes were used to represent the fields in the uniform waveguide sections while the FEM was used to model the locally anisotropic and inhomogeneous regions.

Finally, In section IV, the technique is applied to the horns shown in Figs. 3 and 8. Comparisons with measured data are made.

## II. PROBLEM DESCRIPTION

Consider the generic horn in Fig. 1. As usual, the original three dimensional electromagnetic problem may be reduced to a series of uncoupled two dimensional problems by expanding out the azimuthal variable,  $\phi$ , in a Fourier series. Fig. 2 then shows the computational domain which must be solved for each azimuthal harmonic of interest.

Clearly, the mesh in Fig. 2 has two disjoint boundaries,  $S_1$  and  $S_2$ . Consider  $S_1$ . When revolved about the axis of rotation, the surface generated by  $S_1$  completely envelopes the mesh. It is on this boundary that an integral equation is applied to couple the fields within the finite element region to the external radiation fields. The other boundary,  $S_2$ , consists of two separate parts. One part of this surface,  $S_{2A}$ , is made perpendicular to the z-axis and extends from  $\rho = 0$  to  $\rho = a$ . The surface of revolution generated by this line segment corresponds to a disk spanning the throat of the horn and it is on this mesh boundary that the finite element region is coupled to waveguide modes. The remainder of the surface,  $S_{2B}$ , is made conformal to both the inside and outside walls of the horn. As a result, all metal edges which may contribute to diffraction are included in the finite element mesh. Note that the  $S_{2A}$  surface is placed at  $z = 0$ . This can always be done as the geometry is translationally invariant in the  $z$  direction.

Our subsequent discussion will be concerned only with the FEM/modal coupling via the  $S_{2A}$  mesh boundary.

### III. FORMULATION

The coupling of the waveguide modes to the finite element region is accomplished by two weak-form integral equations (IE). These two IE must be tested properly in order to generate a symmetric system matrix. Hence, in this section, we will state these two IE, show the appropriate test Vectors, then show and discuss the resultant system.

The first key weak-form IE may be obtained by conjugate testing the electric field wave equation with the set of finite element basis functions, denoted here by  $w$ ,

$$w = e^{FEM}, \quad \text{for } i = 1, 2, \dots, N_{FEM}. \quad (1)$$

As in [7,9], these FEM basis functions are chosen such that first order node (edge) based vector functions are used to expand the  $\phi$  (transverse to  $\phi$ ) directed field components. The resulting IE is

$$\begin{aligned} \int_V \frac{1}{\mu_r} (\mathbf{v} \times \mathbf{w}^*) \cdot (\mathbf{v} \times \mathbf{E}) dV - \int_V k_0^2 \epsilon_r \mathbf{w}^* \cdot \mathbf{E} dV \\ - j\omega\mu_0 \int_{S_1} \mathbf{w}^* \cdot (\hat{\mathbf{n}} \times \mathbf{H}) dS_1 \\ - j\omega\mu_0 \int_{S_{2A}} \mathbf{w}^* \cdot (\hat{\mathbf{n}} \times \mathbf{H}) dS_{2A} = 0, \end{aligned} \quad (2)$$

where the electric and magnetic fields,  $\mathbf{E}$  and  $\mathbf{H}$ , are unknowns. The relevant part of this equation is the  $S_{2A}$  surface integration term as this surface is identified with the FEM/waveguide interface. On this surface, we expand the magnetic field as series of waveguide modes (see Appendix),

$$\begin{aligned} \mathbf{H}|_{S_{2A}} &= \mathbf{H}^{WG}|_{z=0} \\ &= \sum_{p=1}^{N_{WG}} (a_p - b_p) \mathbf{h}_p^{WG} \\ &= \sum_{p=1}^{N_{WG}} (a_p - b_p) \frac{1}{Z_p^{WG}} (\mathbf{a}_z \times \mathbf{e}_p^{WG}), \end{aligned} \quad (3)$$

which when substituted back into equation (2), clearly couples finite elements to waveguide modes. This coupling, however, is not yet complete as the preceding substitution enforces only the tangential magnetic field continuity across  $S_{2A}$ . To complete the coupling, the continuity of the electric field across  $S_{2A}$  must be enforced:

$$\mathbf{E}^{FEM}|_{z=0} = \mathbf{E}^{WG}|_{z=0}. \quad (4)$$

When conjugate tested with another set of vectors,  $u$ , this equation gives the second key weak-form equation:

$$\int_{S_{2A}} \mathbf{u}^* \cdot \mathbf{E}^{FEM} dS_{2A} = \int_{S_{2A}} \mathbf{u}^* \cdot \mathbf{E}^{WG} dS_{2A}, \quad (5)$$

Finally, the right-hand side excitation vectors,  $a^B$  and  $a^E$ , are given by

$$a^B(i) = \sum_{j=1}^{N_{WG}} a_j B^{EB}(i, j), \quad (11)$$

and

$$a^E(i) = -a_i K^{BB}(i, i). \quad (12)$$

These vectors involve summations over the complete set of waveguide modes as they represent the excitation of a single finite element by the total forward travelling field in the waveguide.

#### IV. NUMERICAL RESULTS

In this section, we will compare measured and simulated data for the two horns shown in Figs. 3 and 8.

The horn shown in Fig. 3 is a Low Gain Antenna (LGA) to be used aboard the NASA/11, Mars Pathfinder spacecraft. It radiates dominant mode RCP and operates with transmit and receive frequencies at 7.175 and 8.425 GHz, respectively. The chokes are used to null out aperture currents at the two operating frequencies thus insuring radiation in a balanced hybrid mode: small axial ratio and low cross polarization. Note the dielectric plug in the aperture and filling the chokes. This is to prevent Martian dust from entering the horn. The relative permittivity of the dielectric material used is 1.07.

The corresponding two dimensional modelling domain, depicted in Fig. 4, clearly shows where the FEM/MoM and the FEM/modal boundary surfaces are located. This region was meshed using approximately 35 linear nodes per wavelength at the highest frequency of simulation, 8.6 GHz, and 8 waveguide modes of azimuthal index,  $n = 1$ , were allowed to exist at the FEM/modal interface. It is noted that this choice of mesh density and modal content yields a highly converged solution as a mesh of 25 nodes per wavelength and 4 waveguide modes yielded identical far field radiation patterns and reflection coefficients that differed by only 0.3 dB at the -20 dB level. A matrix of order  $N = 5073$  results.

Fig. 5 shows the calculated and measured reflection coefficient over a band of frequencies extending from 7.0 GHz to 8.6 GHz. The measured coefficient was not time gated and thus includes the combined effects of a reflection due to the horn with a reflection due to a polarizer used to transition from rectangular to circular waveguide. The polarizer is, however, placed far enough behind the back of the horn such that the evanescent higher order modes generated do not couple into and through the horn. Figs. 6 and 7 show the far field patterns at 7.175 GHz and 8.425 GHz. Good agreement may be stated.

The method is now applied to the wide band horn antenna shown in Fig. 8. This horn was designed by Philip Stanton of the Jet Propulsion Laboratory to

operate from 5.5 - 10.0 GHz. It features corrugations to equalize the E- and H-plane patterns and a dielectric surface wave element for frequency independent beamwidth over the whole band. To obtain a good match, the corrugations were ring-loaded at the back-end of the horn, tapered through the mid-section, then flanged at the aperture. The computational domain for this horn is shown in Fig. 9. Note that the FEM/modal boundary is placed just behind the back of the surface wave element inhomogeneity.

The horn was simulated once with LCP excitation ( $n = -1$ ) then again with RCP excitation ( $n = 1$ ). The results from these two runs were combined to generate the linear E- and H-plane patterns shown. For these simulations, the computational domain was meshed at a linear density of approximately 31 nodes per wavelength at the highest frequency of simulation thus giving rise to a system matrix of order  $N = 37,427$ . Again, it is noted that this high mesh density was chosen in order to guarantee that the solution obtained has already converged.

Fig. 10 shows the measured reflection coefficient over the whole band and the calculated value at a discrete set of frequencies. The measured coefficient was time gated to remove a reflection from the orthomode junction used to transition from coax to waveguide. Although this junction does excite higher order modes, these evanescent modes do not couple into and through the horn as this discontinuity is located far behind the track of the horn. Fig. 11 shows the far field pattern at 8.2 GHz. Far field patterns at other frequencies over the band also show good agreement. For comparison, Fig. 12 shows the far field pattern of the horn without dielectric surface wave element at the same frequency, 8.2 GHz. Note that the E- and H-plane patterns are not coincidental when the surface-wave element is absent.

## APPENDIX

The fields in the waveguide are written as:

$$\mathbf{E}^{WG} = \sum_{p=1}^{N_{WG}} a_p \mathbf{e}_p e^{-jk_{z,p}z} + b_p \mathbf{e}_p e^{+jk_{z,p}z} \quad (13)$$

$$\mathbf{H}^{WG} = \sum_{p=1}^{N_{WG}} a_p \mathbf{h}_p e^{-jk_{z,p}z} - b_p \mathbf{h}_p e^{+jk_{z,p}z} \quad (14)$$

where  $a_p$  ( $b_p$ ) are the expansion coefficients for the forward (backward) modes in the guide. The transverse mode vectors in equations (13) and (14) are given by

$$\mathbf{e}_p^{TM} = j \sqrt{\frac{|k_{z,p}|}{\omega \epsilon \pi}} \frac{J'_n\left(\frac{x_{np}}{a}\right)}{a J_{n+1}(x_{np})} e^{+jn\phi} \mathbf{a}_\rho$$

$$= \sqrt{\frac{|k_{z,p}|}{\omega \epsilon \pi}} \frac{n}{x_{np}} \frac{J_n(\frac{x_{np} \rho}{a})}{\rho J_{n+1}(x_{np})} e^{\pm j n \phi} \mathbf{a}_\phi \quad (15)$$

$$\mathbf{h}_p^{TM} = \frac{\omega \epsilon}{k_{z,p}} (\mathbf{a}_z \times \mathbf{e}_p^{TM}) = \frac{1}{Z_p^{TM}} (\mathbf{a}_z \times \mathbf{e}_p^{TM}) \quad (16)$$

$$\begin{aligned} \mathbf{e}_p^{TE} = & \mp j \sqrt{\frac{\omega \mu}{|k_{z,p}| \pi}} \frac{n}{\sqrt{x_{np}'^2 - n^2}} \frac{J_n(\frac{x_{np}' \rho}{a})}{\rho J_n(x_{np}')} e^{\pm j n \phi} \mathbf{a}_\rho \\ & + \sqrt{\frac{\omega \mu}{|k_{z,p}| \pi}} \frac{x_{np}'}{\sqrt{x_{np}'^2 - n^2}} \frac{J_n'(\frac{x_{np}' \rho}{a})}{a J_n(x_{np}')} e^{\pm j n \phi} \mathbf{a}_\phi \end{aligned} \quad (17)$$

$$\mathbf{h}_p^{TE} = \frac{k_{z,p}}{\omega \mu} (\mathbf{a}_z \times \mathbf{e}_p^{TE}) = \frac{1}{Z_p^{TE}} (\mathbf{a}_z \times \mathbf{e}_p^{TE}) \quad (18)$$

where  $a$  is the waveguide radius and

$$\begin{aligned} k_{z,p}^{TE} &= k_0^2 - \frac{x_{np}'^2}{a^2} \\ k_{z,p}^{TM} &= k_0^2 - \frac{x_{np}^2}{a^2} \end{aligned}$$

These vectors are nearly identical to the standard set given in Marcuvitz [1] but differ in three important respects. First, these mode vectors are written as harmonics of the azimuthal angle,  $\phi$ . Second, the choice of phase on the mode vectors is not arbitrary. In order to generate a symmetric system matrix (8), the  $z(\rho)$  components of  $\mathbf{e}_p^{WG}$  must be purely real (imaginary) for both propagating and evanescent modes. This point is explained in [7] and has to do with the choice of finite element basis function. q'bird, these mode vectors satisfy power orthonormalization:

$$\int_S \mathbf{e}_m \times \mathbf{h}_n^* dS = \begin{cases} \delta_{mn}, & \text{for propagating modes} \\ -j\delta_{mn}, & \text{for evanescent TM modes} \\ j\delta_{mn}, & \text{for evanescent TE modes} \end{cases}$$

This normalization is convenient for S parameter calculations.

#### ACKNOWLEDGEMENT

The authors would like to thank: Dr. Michael L. Oberhart, Tommy Y. Otoshi and Philip H. Stanton for the use of their horns, data and for many useful discussions; Joe L. Garland, Harry F. Reilly, Robert F. Thomas and Phillip A. Yates for their measurement expertise; and Dr. Hugh K. Smith for insightful discussions.

Support for this computing research was provided by the J11, Supercomputing Project on the CRAY computers at the Jet 1 'repulsion Laboratory and at

Goddard Space Flight Center. The JPL Supercomputing Project is sponsored by the Jet Propulsion Laboratory and the NASA Office of Space Sciences and Applications.

## References

- [1] R. C. Johnson and H. Jasik, *Antenna Engineering Handbook, 2nd Ed.*, New York, Mc-Graw Hill Book Company Inc., 1984, pp. 15.28 - 15.36.
- [2] P. J. B. Clarricoats and A. D. Olver, *Corrugated Horns for Microwave Antennas*, London, IEE Books, 1984.
- [3] A. W. Rudge, K. Milne, A. D. Olver, and P. Knight, *The Handbook of Antenna Design, Vol. 1*, London, IEE Books, 1982, pp. 549-560.
- [4] E. Lier, "A dielectric hybrid mode antenna feed: A simple alternative to the corrugated horn," *IEEE Trans. Antennas and Propagation*, vol. 34, no. 1, pp. 21-29, Jan. 1986.
- [5] A. Berthon and R. P. Bills, "Integral equation analysis of radiating structures of revolution," *IEEE Trans. Antennas and Propagation*, vol. 37, no. 2, pp. 158-170, Jan. 1989.
- [6] X. Yuan, D. R. Lynch, and J. W. Strohbehn, "Coupling of finite element and moment methods for electromagnetic scattering from inhomogeneous objects," *IEEE Trans. Antennas and Propagation*, vol. 38, no. 3, pp. 386-393, March 1990.
- [7] D. J. Hoppe, L. W. Epp, and J. F. Lee, "A hybrid symmetric FEM/MOM formulation applied to scattering by inhomogeneous bodies of revolution," *IEEE Trans. Antennas and Propagation*, vol. 42, no. 6, pp. 798-805, June 1994.
- [8] L. W. Epp, D. J. Hoppe, G. C. Chinn and J. F. Lee, "Scattering and radiation from anisotropic, lossy bodies of revolution," in *Abstracts of the 1994 Progress in Electromagnetics Research Symposium*, Noordwijk, The Netherlands.
- [9] K. Ise, and M. Koshiba, "Numerical analysis of H-plane waveguide junctions by combination of finite and boundary elements," *IEEE Trans. Microwave Theory and Techniques*, vol. 36, no. 9, pp. 1343-1351, Sept. 1988.
- [10] G. Wilkins, J. F. Lee, and R. Mittra, "Numerical modeling of axisymmetric coaxial waveguide discontinuities," *IEEE Trans. Microwave Theory and Techniques*, vol. 39, no. 8, pp. 1323-1328, Aug. 1991.

- [11] N. Marcuvitz, *Waveguide Handbook*, New York, Mc-Graw Hill Book Company Inc., 1951, pages 66-69.



## Figure Titles

Fig. 1. Generic axisymmetric horn.

Fig. 2. Computational domain for horn shown in Figure 1.

Fig. 3. Pathfinder spacecraft low gain horn antenna (LGA).

Fig. 4. Computational domain for Pathfinder LGA.

Fig. 5. Measured and calculated reflection coefficient for Pathfinder LGA.

Fig. 6. Pathfinder LGA far field pattern at  $f = 7.175$  GHz.

Fig. 7. Pathfinder LGA far field pattern at  $f = 8.425$  GHz.

Fig. 8. Prime focus feed horn (PFF) with coaxial surface wave element (SWE).

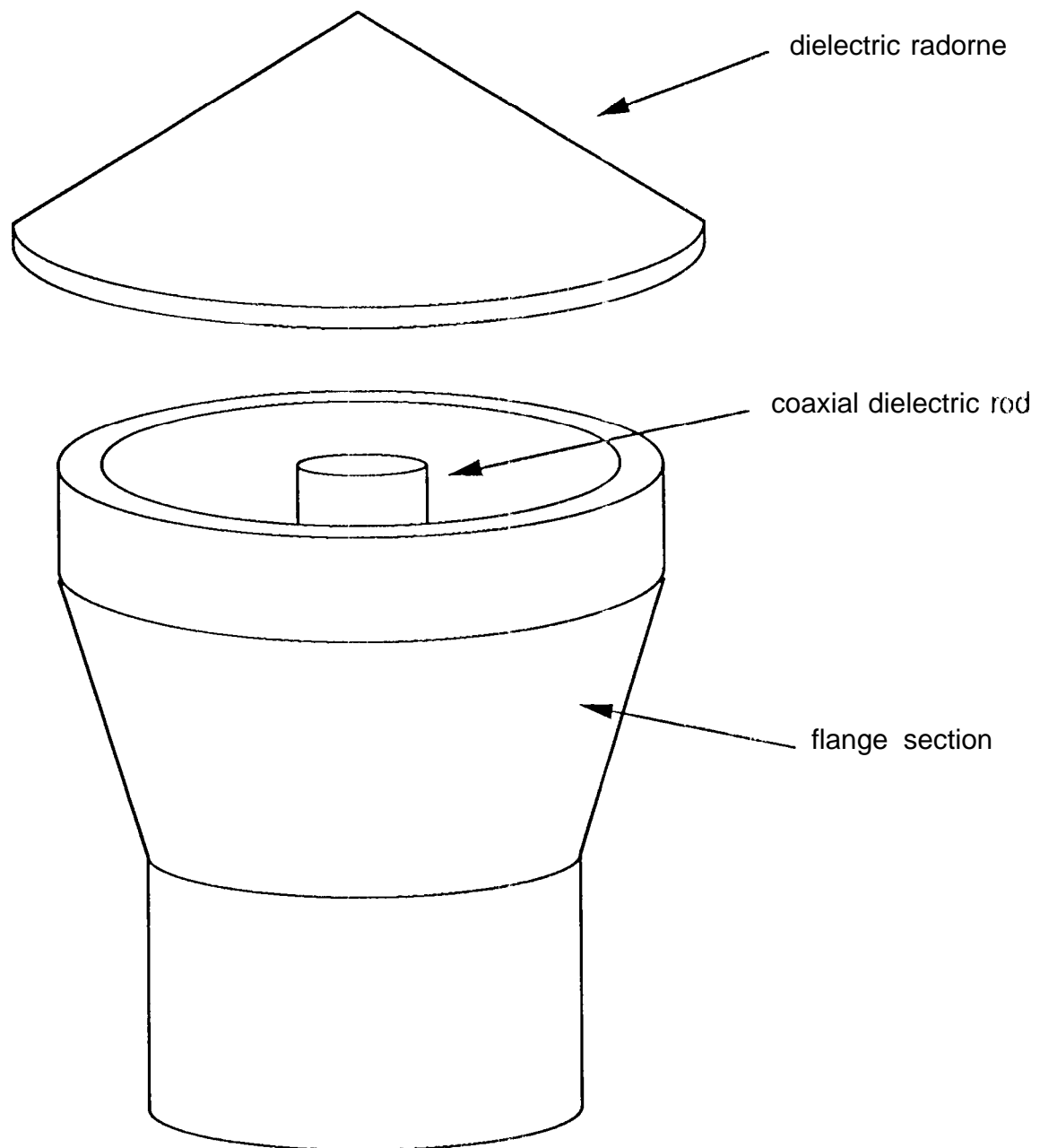
Fig. 9. Computational domain for PFF horn.

Fig. 10. Measured and calculated reflection coefficient for PFF horn with SWE.

Fig. 11. Far field pattern for PFF horn with SWE at  $f = 8.2$  GHz.

Fig. 12. Far field pattern for PFF horn without SWE at  $f = 8.2$  GHz.

Figure 1. Generic horn with axial symmetry



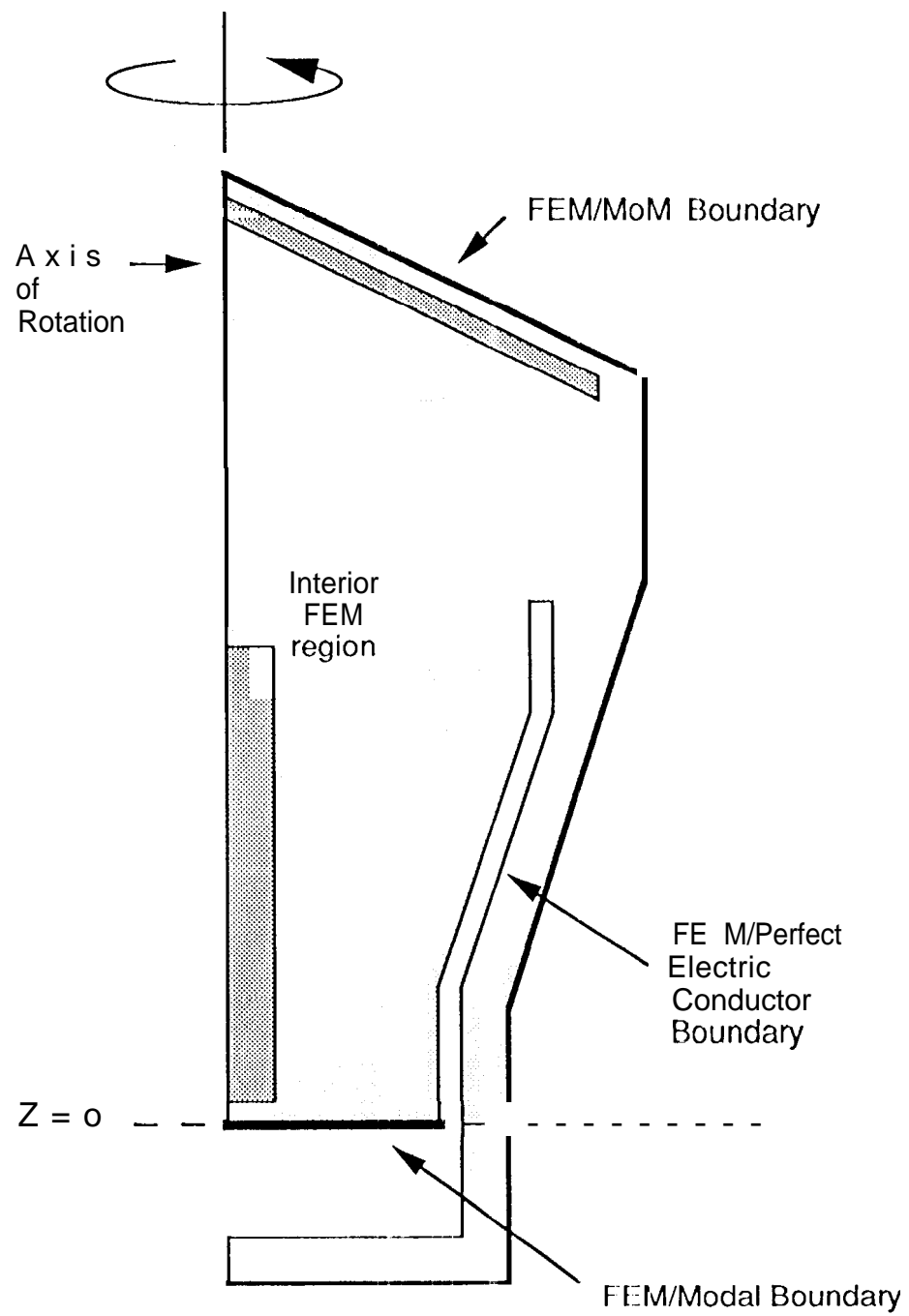


Figure 2. Computational domain for horn shown in Fig. 1.

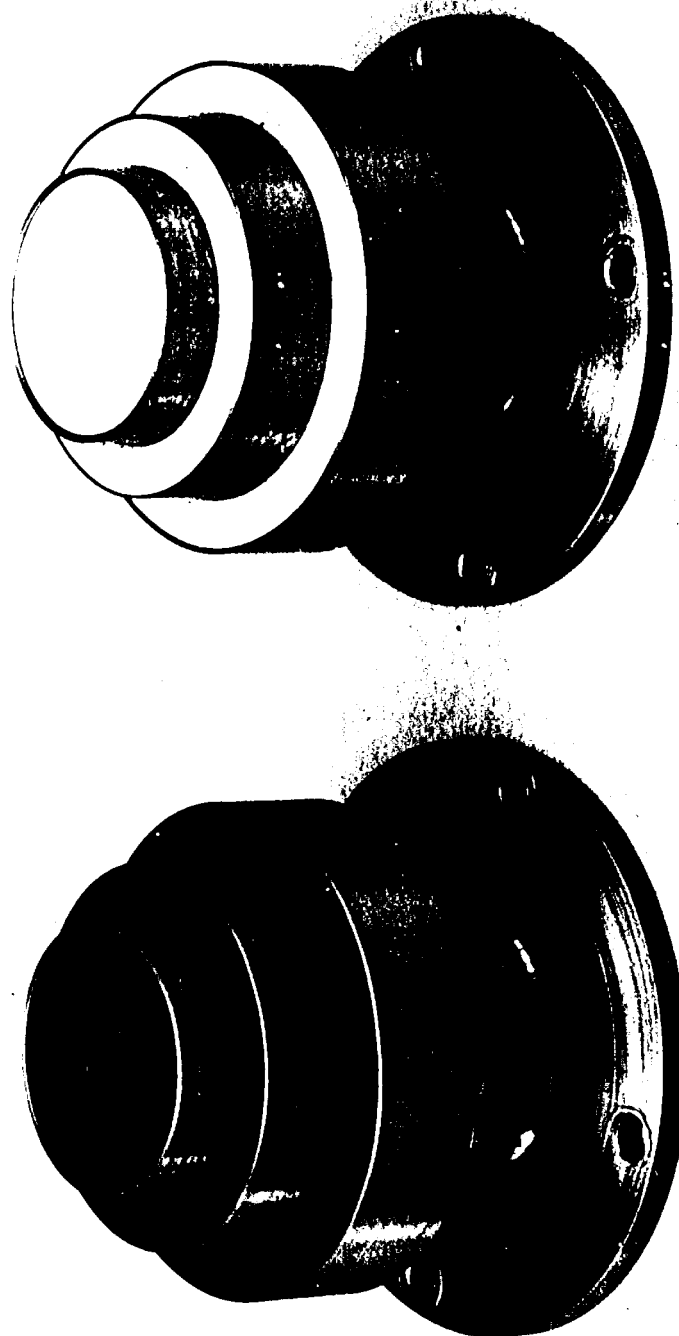


Figure 3. Pathfinder Low Gain Antenna Horn (LGA)

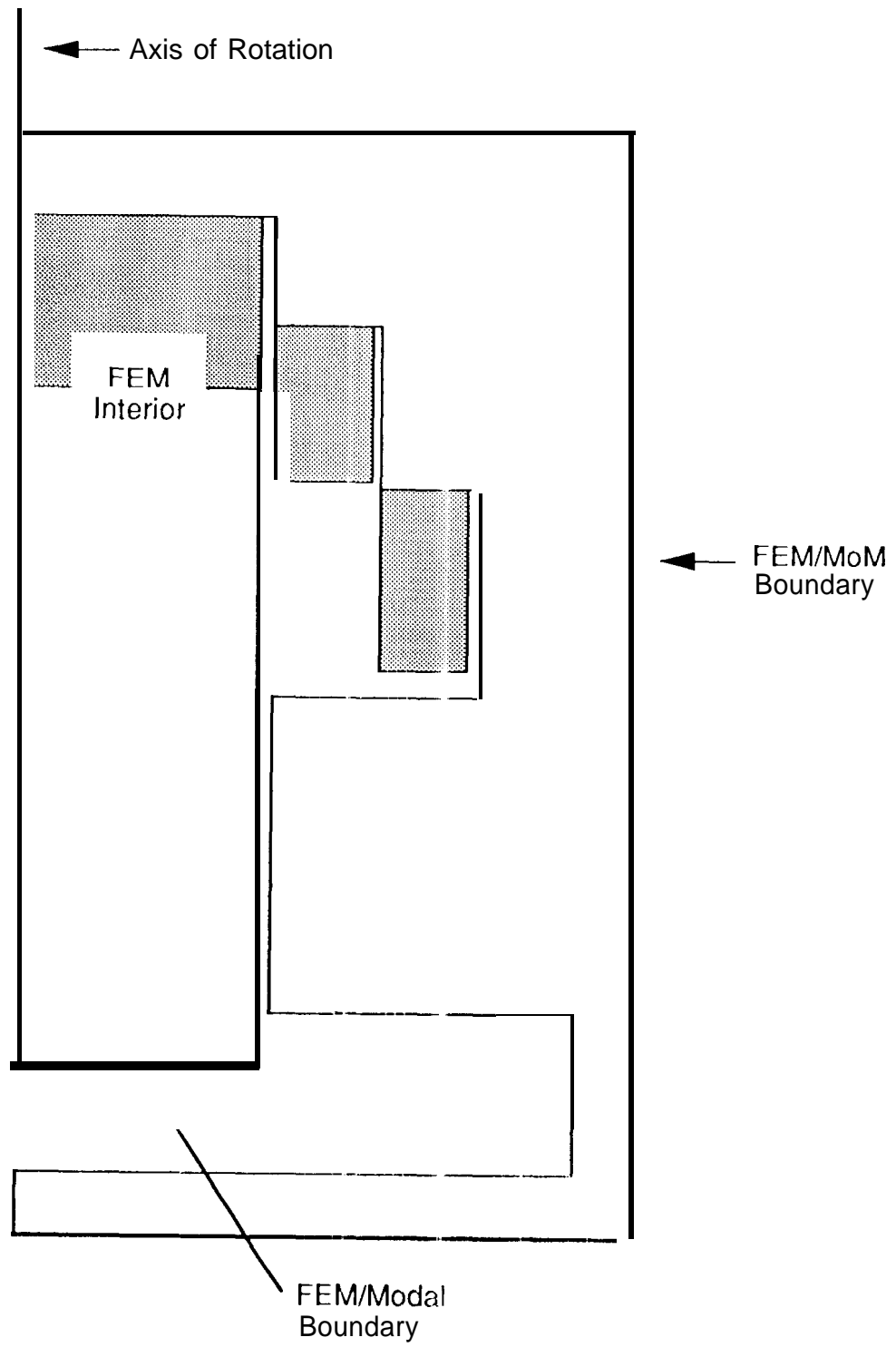
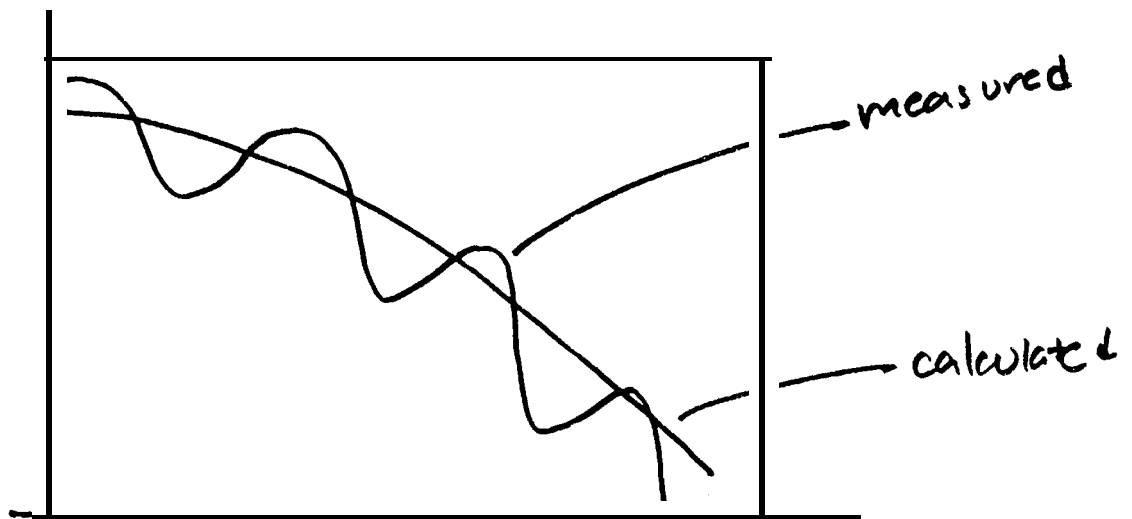
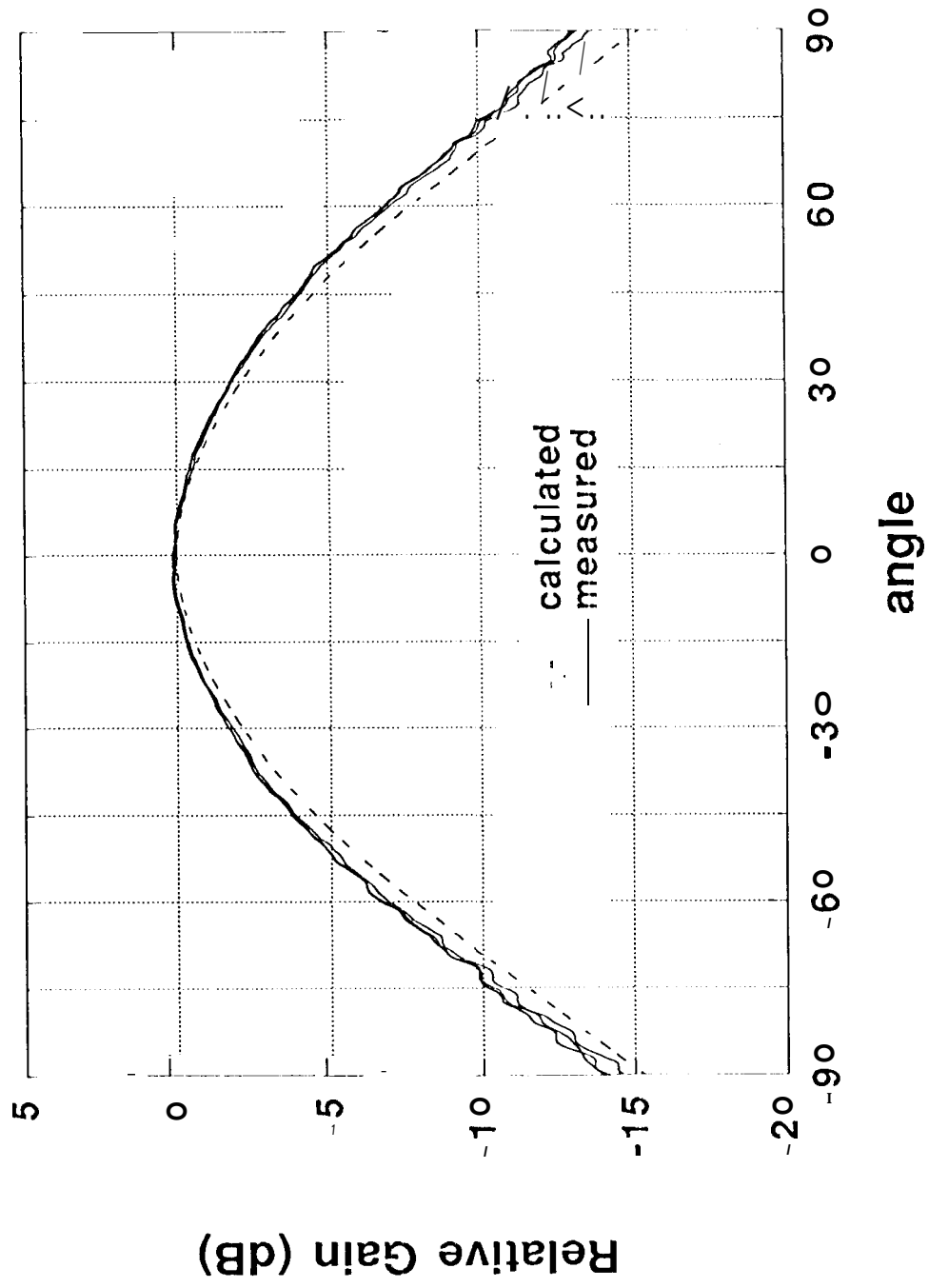


Figure 5. - "comparison of measured & calculated reflection coefficient for Pathfinder LGA<sup>™</sup> horn" is still being prepared.

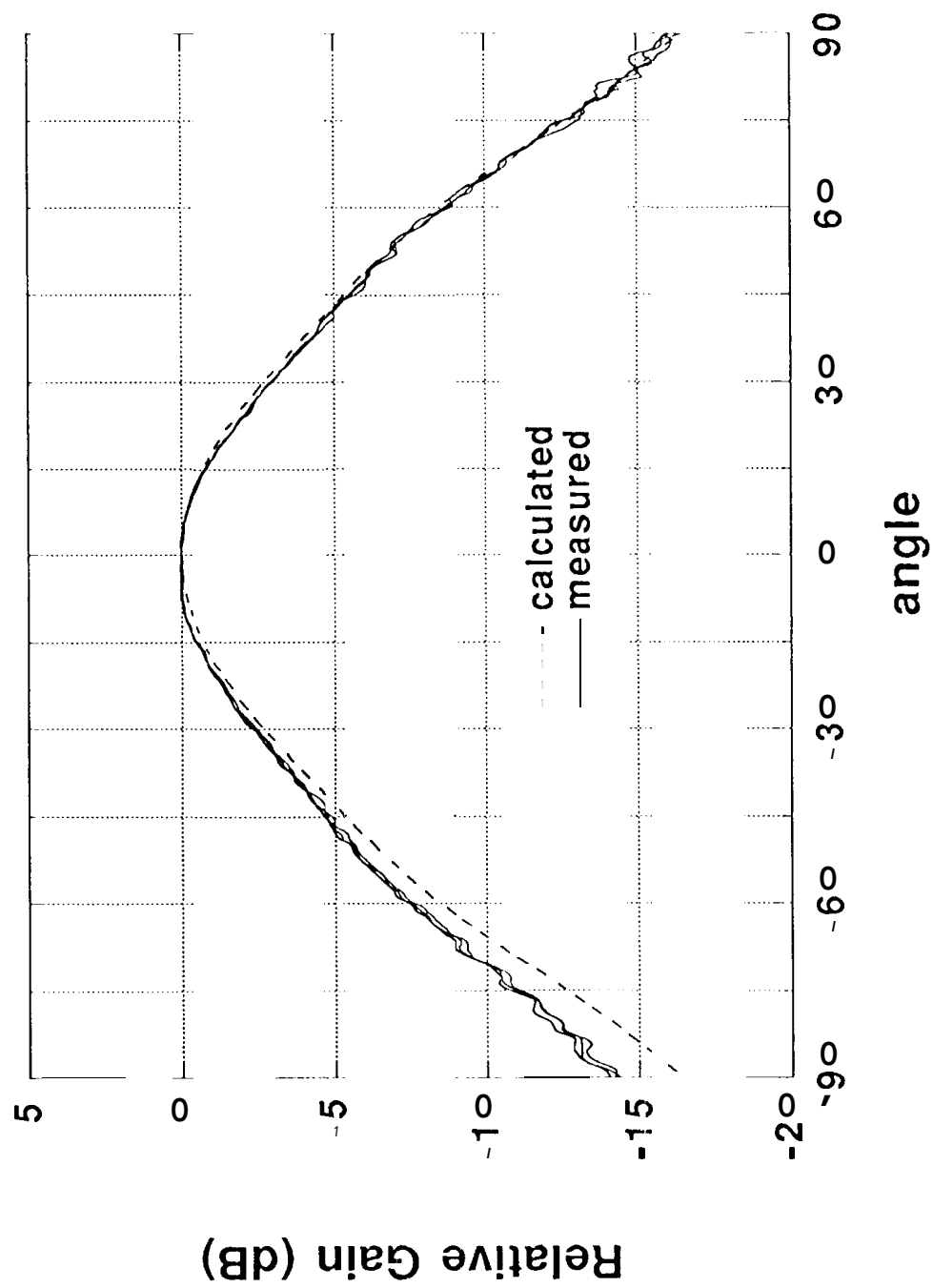


(see body of paper for explanation of ripple in measured pattern)

Pathfinder LGA far-field pattern:  
co-pol at  $f = 7.175$  GHz



Pathfinder LGA far-field pattern:  
co-pol at  $f = 8.425$  GHz





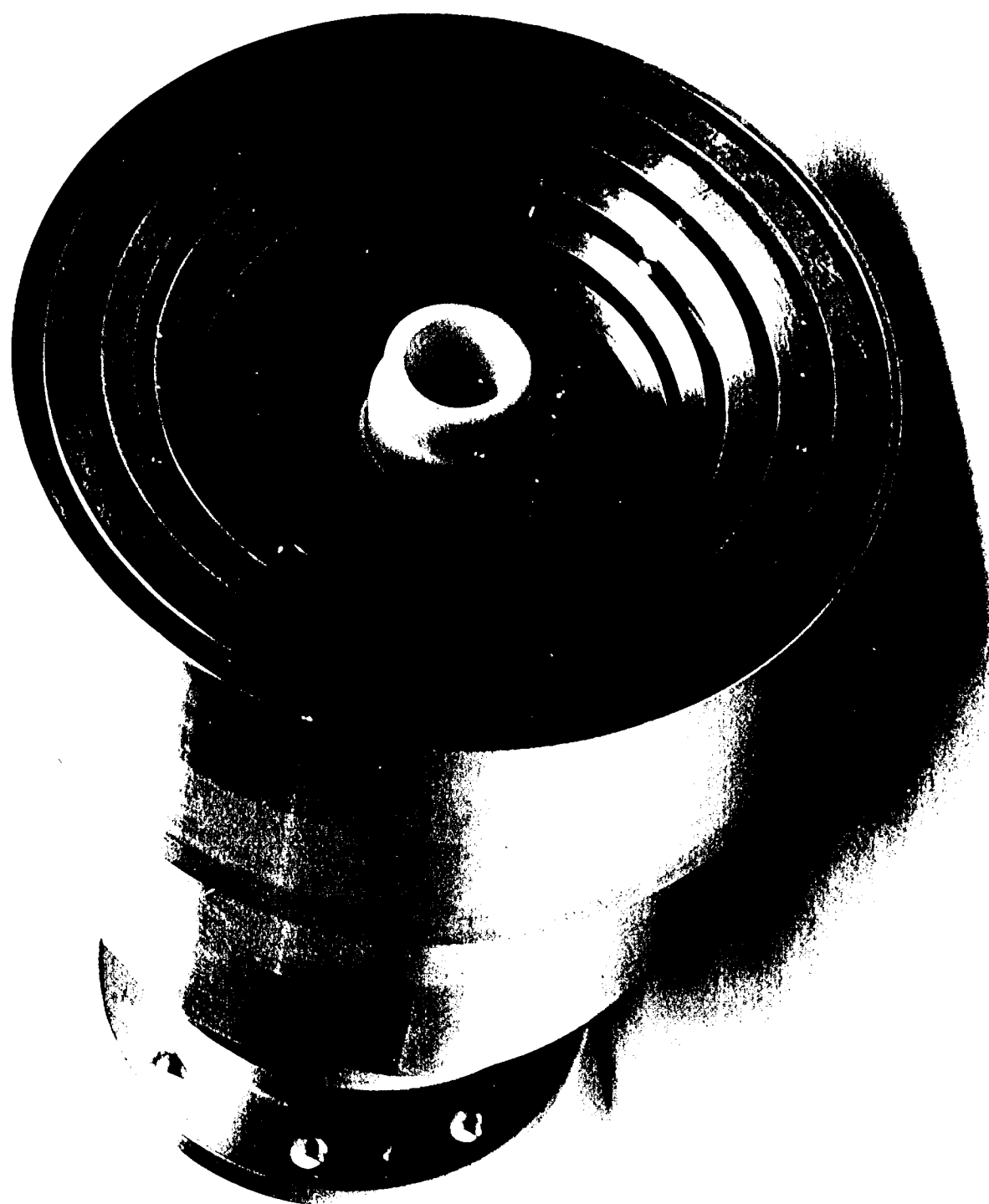
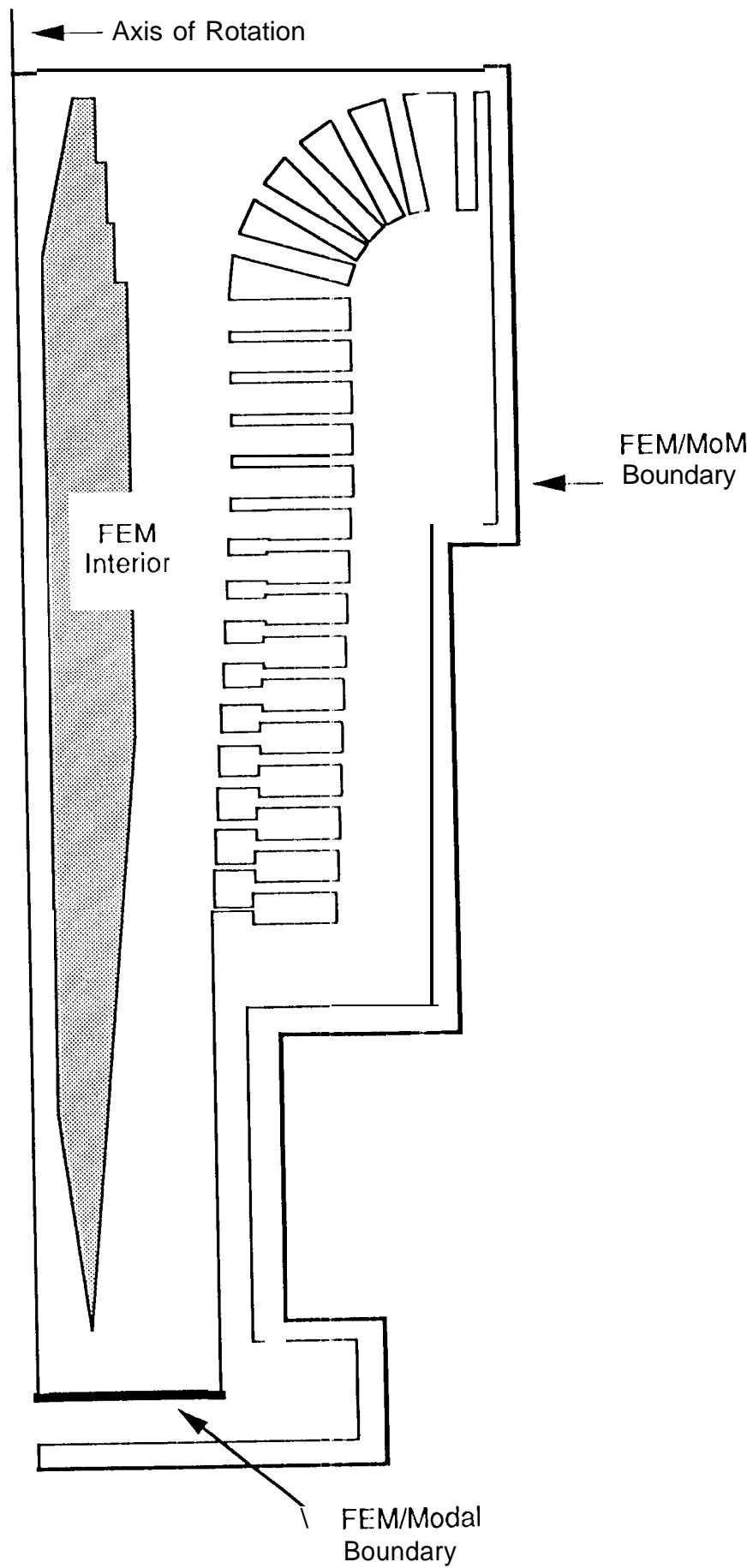
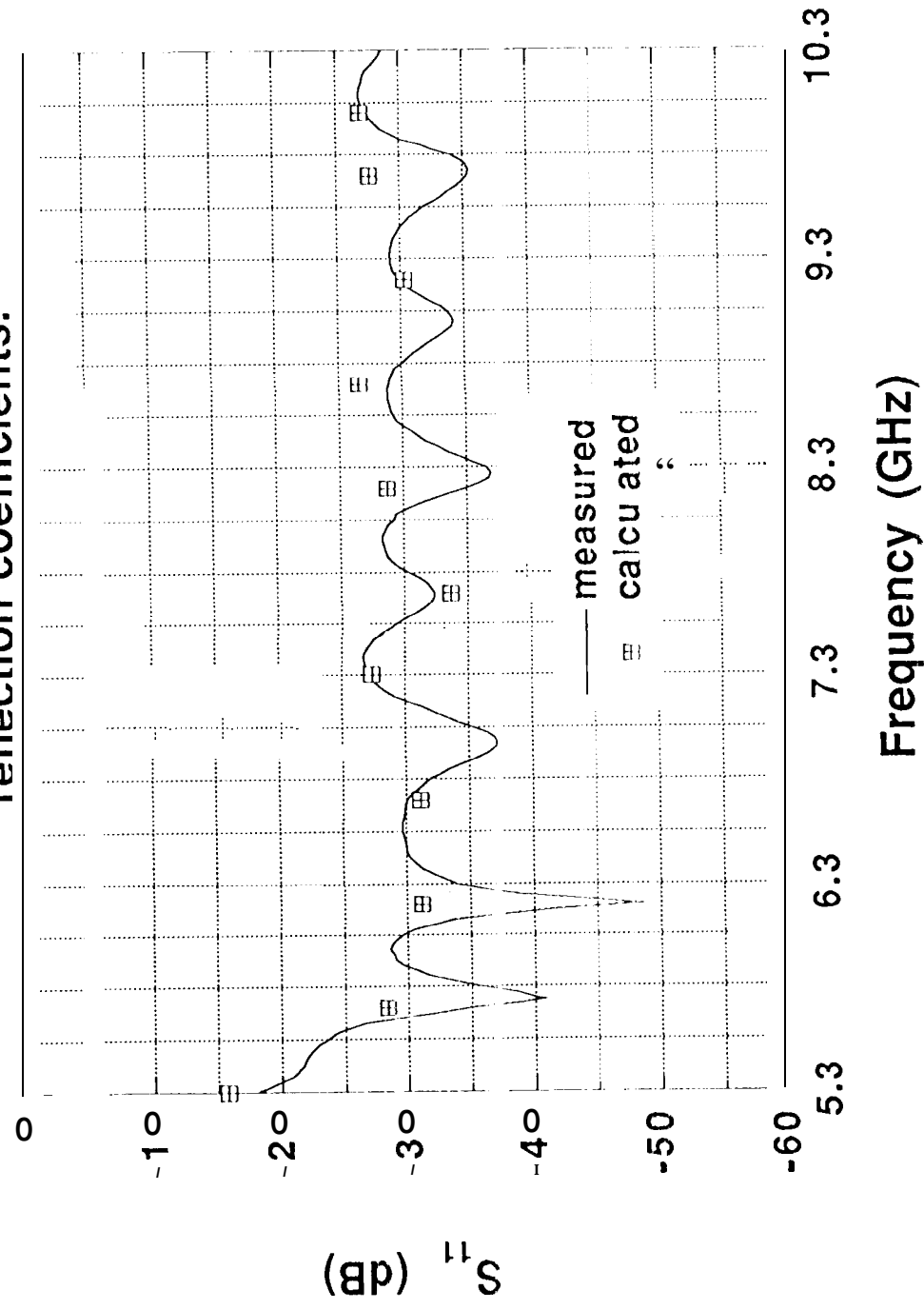


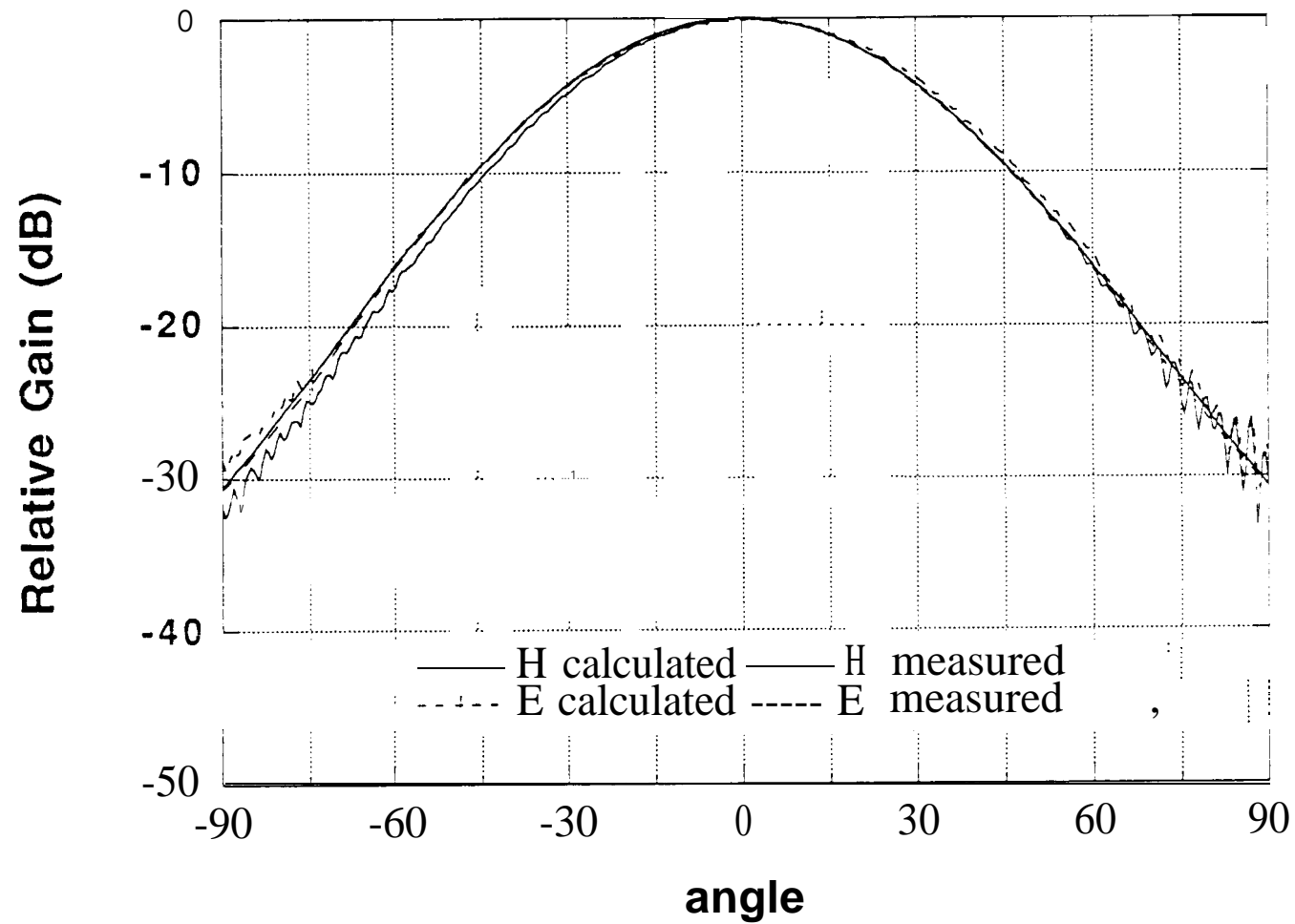
Figure 8. Prime Focus Feed Horn with SWE.



PFF horn:  
comparison of measured and calculated  
reflection coefficients.



**PFF horn:  
far-field patterns at  $f = 8.2$  GHz**



**PFF horn without SWE:  
far-field patterns at  $f = 8.2$  GHz**

